A study on the geometry of dislocation patterns in the surrounding of nanoindents in a TWIP steel using electron channeling contrast imaging and discrete dislocation dynamics simulations

J.-l. Zhang, S. Zaefferer *, D. Raabe

Max-Planck-lnstitut für Eisenforschung, Max-Planck-Straße 1, D-40237 Düsseldorf, Germany

ABSTRACT

Electron channeling contrast imaging under controlled diffraction conditions (cECCI) enables observation of crystal defects, especially dislocations, stacking faults and nano-twins, close to the surface of bulk samples. In this work cECCI has been employed to observe defects around nanoindents into the surface of {100}-, {110}-, {111}-oriented grains in a Fe–22Mn–0.65C (wt%) TWIP steel sample (fcc crystal structure, stacking fault energy $\sim$20 mJ/m²) using a cone-spherical indenter. The dislocation patterns show four- and two-fold symmetries for the {100}- and {110}-orientation, and a three-fold symmetry for the {111}-orientation which is, however, difficult to observe. Discrete dislocation dynamics (DDD) simulations of the indentation were carried out to complement the static experimental investigations. The simulations were carried out with both, cross-slip disabled and enabled conditions, where the former were found to match to the experimental results better, as may be expected for an fcc material with low stacking fault energy. The 3-dimensional geometry of the dislocation patterns of the different indents was analysed and discussed with respect to pattern formation mechanisms. The force–displacement curves obtained during indentation showed a stronger strain hardening for the {111} oriented crystal than that for the other orientations. This is in contrast to the behaviour of, for example, copper and is interpreted to be due to planar slip. Irrespective of orientation and indentation depth the radius of the plastically deformed area was found to be approximately 4 times larger than that of the indenter contact area.

1. Introduction

Instrumented nanoindentation is an excellent tool for characterising the mechanical properties and the deformation behaviour of materials at nano/micro-scales [1,2]. The mechanical data, such as hardness and elastic modulus, obtained by nanoindentation are, however, not easily interpretable in terms of macroscopic mechanical properties because of the complex stress and strain field developed during the test. Although numerous studies were carried out to understand the strain field formed beneath and besides the indenter, a number of questions about the associated dislocation activities are still unresolved. It is known, for example from 3D EBSD investigations, that fields of different crystallographic rotations are formed below an indent [3,4]. Transmission electron microscopy (TEM) observations of nanoindentation provided detailed information of the mechanisms associated with localized deformation [5,6]. All these experimental investigations

have certain limitations though: The 3D EBSD observations reveal the existence of geometrically necessary dislocations in terms of the detected rotation patterns but fail to show the actual complete deformation pattern in terms of the underlying dislocations. TEM observations show the true dislocation arrangements but they suffer from the fact that thin foils have to be used for that and, hence, either lateral or depth directional information cannot be obtained. To a certain extent the missing information can be complemented by crystal plasticity simulations, as have been carried out in some studies [3–5]. This approach, however, suffers from adjustable parameters such as latent hardening and cross hardening parameters, and uncertainties associated with boundary condition treatment such as friction.

A significant number of investigations have been reported on the crystallographic orientation induced patterns around nanoindents in materials with fcc structure [7–13]. Most of the works were conducted by comparison of finite element simulations with secondary electron (SE) images or atomic force microscopy (AFM) profiles [9,11]. Irrespective of the shape of the indenter used in these studies, four- and two-fold symmetries for {100}- and {110}-oriented crystals were reported. For {111}-oriented crystals both,

six-fold [9] and three-fold [11] symmetries were suggested. In these works the surface topographical pile-up or sink-in patterns were used for comparison between simulation and experimental results. However, detailed information on how these patterns are actually formed in terms of the underlying dislocation activities was not provided.

In addition, the variation of hardness and/or elastic modulus with indentation depth, the so called indentation size effect, raises a lot of difficulties with obtaining real values of the mechanical properties. In order to understand the size effect numerous studies have been carried out in investigating the size of the plastic deformation zone as a function of the indentation depth and/or indenter size [14–16]. Most of the works were done by numerical calculations or by topographical pile-up or sink-in pattern observations using atomic force microscopy (AFM) and scanning electron microscopy (SEM). Also, the real lateral extension of the plastic deformation zone was not sufficiently studied in detail yet.

In order to overcome some of the mentioned experimental and simulation difficulties we used a newly designed technique, referred to as electron channeling contrast imaging under controlled diffraction conditions (cECCI). It allows the direct observations of crystal defects like dislocations or stacking faults close to the surface of bulk samples [17–19]. This technique, which has similarities to dark field TEM, is applied in an SEM and allows probing approximately the first 50–100 nm of material below the surface [20].

In the present work we applied the cECCI technique to study dislocation structures in the surrounding of nanoindents in a steel with twinning induced plasticity (TWIP) and fcc crystal structure. Nanoindentation was carried out either in a load-controlled mode with a maximum load or in displacement-controlled mode up to different indentation depths on {100}- {110}- and {111}-oriented grains in a polycrystalline specimen. The aim of the study is to understand in more detail the formation of the defects below and next to the indent and to contribute in this way to a better understanding of the pattern formation process. In order to be able to interpret our experimental results we also applied discrete dislocation dynamics (DDD) simulations using the Parallel Dislocation Simulator (ParaDiS) code [21], which shows, to a certain extent, which slip systems are active and what the shape and the type of the resulting dislocations in the network is. These data were compared with our experimental results.

2. Methodology

2.1. Material and sample preparation

A Fe–22Mn–0.65C (wt%) TWIP steel (stacking fault energy is around 20 mJ/m^2) was melted in an induction furnace under Ar atmosphere and cast into a block with square shaped cross section. The ingot was hot rolled and homogenised at 1100 °C to form a homogeneous, virtually strain free single fcc phase microstructure with an average grain size of 150 μm. Because an optimum surface preparation is essential for both nanoindentation [22] and ECCI, sample preparation had to be done with great care. In this work the sample surface was wet-ground, diamond polished, and later polished with colloidal silica. A slight etching with a solution of 90% H_2O_2 and 10% HF for 10 s or 15 s was then carried out in order to remove any deformation layer produced during previous polishing steps. EBSD was conducted using an EDAX/TSL system and a Hikari camera for obtaining the orientation of each grain. Grains with misorientations of less than 3° with respect to {100}-, {110}-, {111}-surface normals were selected. These grains were marked by milling crosses into neighbouring sites using a focused ion beam (FIB) with an accelerating voltage of 30 kV. FIB milling

was done under careful avoidance of ion-beam exposition of the areas previewed for nanoindentation in order to prevent the specimen surface from Ga^+ beam damage, which could be fatal to both the deformation during nanoindentation [23] and the formation of electron channeling contrast (ECC) [24].

2.2. Nanoindentation testing and contact mechanics

A Hysitron TriboScope 950 nano-indenter system was used for nano-hardness testing. The system contained a XYZ sample stage and a setup which combines a piezo-scanner with a transducer and a diamond indenter tip with variable geometries. The XYZ sample stage was used for the fine positioning of the FIB marked area on the sample surface under the piezo-scanner as well as for the approach of the indenter in surface normal direction.

A cone-spherical indenter with a tip angle of 90° and tip radius of 1.4 μm was used. This indenter shape was selected to avoid non-crystallographic symmetries [1]. The tests were conducted with either maximum applied load of 1000 μN in load-controlled mode or with various maximum applied depths of 40 nm, 50 nm, 60 nm, 70 nm, 80 nm, 90 nm and 100 nm in depth-controlled mode. A trapezoid loading-unloading profile was used with a holding time of 10 s at the maximum load or depth. A matrix of 10 × 10 indents with a spacing of 10 μm was used for each of the experiments.

Load and displacement were measured simultaneously during indentation. In order to calculate accurate values for both hardness and Young's modulus [25], the exact geometry of the indenter tip is required. Standard calibration was performed beforehand at various depths on quartz.

2.3. Electron channeling contrast imaging (ECCI)

ECC images of each indent were captured using a dual-beam Zeiss-Crossbeam instrument XB 1540 (Carl Zeiss SMT AG, Germany) consisting of a Gemini-type field emission gun (FEM) electron column and a focussed ion beam (FIB) device. The Gemini electron column is particularly suited for ECCI because of its small beam convergence angle of about 5 mrad or smaller. The backscatter signal is obtained on a solid-state silicon four-quadrant backscatter electron detector with a diameter of approximately 10 mm, positioned directly below the pole piece. The sample surface is positioned close to perpendicular to the electron beam in order to obtain a strong backscattering signal. The correct contrast conditions for defect observations are obtained by positioning the sample in so-called two-beam conditions where only one set of lattice planes in the crystal is positioned close to their Bragg angle. To this end the sample stage is rotated up to ± 180° and/or tilted up to about 20° The necessary tilt and rotation angles are obtained, as it was proposed by Gutierrez et al. [17], by measuring, in a first step, the orientation of the grain under consideration using the EBSD technique. This orientation is then imported into the software TOCA [26] for simulating electron channeling patterns. The user applies this software to determine the tilt and rotation angle necessary to obtain two-beam conditions with a high-intensity diffraction reflection. In fact, the centre of an experimental or simulated channeling pattern represents the crystallographic direction of the primary electron beam during imaging, thus indicating the active diffraction conditions. In the present work this centre is marked by a white cross in the simulated patterns in Fig. 2(c), (f), and (i). Depending on the surface conditions of the sample, accelerating voltages of 15 kV, 20 kV and 25 kV were used for getting optimum contrast for ECCI. A working distance of around 6 mm was used to increase the backscatter electron signal collected by the detector.

All experimental results presented in the following depend on the correct setting of suitable channeling conditions. Before

anything else we will therefore discuss the accuracy of the here presented technique.

2.4. Accuracy of channeling conditions

As discussed in detail in [20] positioning of the sample into two-beam diffraction conditions (also called channeling conditions) based on EBSD measurements is afflicted with various errors, including the inaccuracy inherent to EBSD orientation measurements, inaccuracy of sample tilt and of relative stage-detector positioning. These errors add up to a maximum of about 2°, occurring about any possible rotation axes. As a result, the desired diffraction conditions can only be approximated with the technique described above.

The red circles traced around the calculated diffraction conditions in Fig. 2(c), (f) and (i) have a radius of 2° and illustrate the inaccuracy that has to be expected. After the sample has been brought to these approximate diffraction conditions the sample is tilted further by a maximum of 2° under BSE observation until a minimum BSE intensity of the area under observation indicates that channeling conditions have been reached. In most cases this situation is then less than 0.5° away from the correct channeling conditions. It should be noted, however, that there are cases where the wrong diffraction vector is accidentally chosen. This may particularly happen close to prominent zone axes of channeling patterns, where several diffraction vectors with good channeling contrast are closely spaced.

2.5. Model description (DDD)

For the discrete dislocation simulations we used the ParaDiS code which was developed at Lawrence Livermore National Laboratory [21]. The method represents a dislocation network in terms of an array of interconnected nodes which have line segments between them. One single stable dislocation node can connect up to four individual segments (dislocation arms). Each of the dislocation segments carries a Burgers vector and is assigned a glide plane normal. The Burgers vector is conserved everywhere in a dislocation network, except for the case of a pinned node with a single arm, such as for instance encountered at the end points of a Frank–Read source. The resulting force exerted on a specific dislocation node due to the elastic stress field exerted by its own dislocation arms and by the elastic stresses of all other dislocation segments in the system is calculated using a non-singular elastic formulation suggested by Cai et al. [27]. The additional nodal force created by the external loading conditions is calculated by using the Peach–Koehler equation. The resulting nodal velocity is proportional to the projected nodal force through a mobility tensor which essentially differentiates between glide and climb. The topology update of such a loaded dislocation network mimics all

relevant motion and collision phenomena that are potentially encountered in a real crystal. Reactions such as annihilation, junction zipping as well as junction unzipping occur through the collisions and dissociations of dislocation nodes [21].

For simulating the current indentation experiments a sample box geometry of 12,000 b × 12,000 b × 1600 b (b being the length of the Burgers vector) was chosen. 5000 time steps were used for loading, 5000 for holding, and 5000 for unloading. The simulations were conducted for crystal orientations [001], [011], and [111]. In order to elucidate the effect of the relatively low stacking fault energy of the material under investigation the simulations were carried out using the related elastic parameters of pure Cu. Simulations were conducted using both, cross-slip disabled and enabled conditions in order to study the effect of the stacking fault energy on the resulting dislocation pattern formation. In accordance with the experimental observations no mechanical twinning was enabled in the simulations.

3. Results

3.1. Dislocation pattern symmetry

An ECC image displays the projection of lattice defects, such as dislocation lines, stacking faults, etc. within the visibility depth below the surface of a bulk sample. Depending on the accelerating voltage, the material type, and the activated diffraction vector, visibility depths of 50–100 nm can be reached [20]. If two-beam conditions are satisfied, an individual dislocation appears as straight or curved white line on a dark background with a bright dot indicating the intersection point with the sample surface and fading contrast with increasing depth below the surface [20,28]. Similarly, a stacking fault appears as a bright area associated to a straight bright line indicating the intersection of the stacking fault plane with the sample surface [20].

Fig. 1 shows examples of the defect state of the investigated sample for different grains before nanoindentation as observed by ECCI, indicating the high heterogeneity of dislocation density in this material. Fig. 1(a) shows a high, (b) a medium and (c) a low defect density. In average the material shows a dislocation density of about 3.5×10^{12} m^{-2} measured as dislocation intersections per surface area. According to stereological relationships [29] the dislocation line length per volume is approximately equal to twice the intersection number per area if the lines are randomly distributed. Thus, the dislocation length per volume density is estimated to around 1×10^{13} m^{-2} for the present material. This is a value comparable to those reported in literature for well-recrystallized microstructures [30].

Fig. 2a, d and g show ECC images of the discrete dislocation patterns around the indents, on the {100}-, {110}- and {111}-

$\rho = 8.5 \times 10^{12}$ m^{-2} $\rho = 4.8 \times 10^{12}$ m^{-2} $\rho = 1.4 \times 10^{12}$ m^{-2}
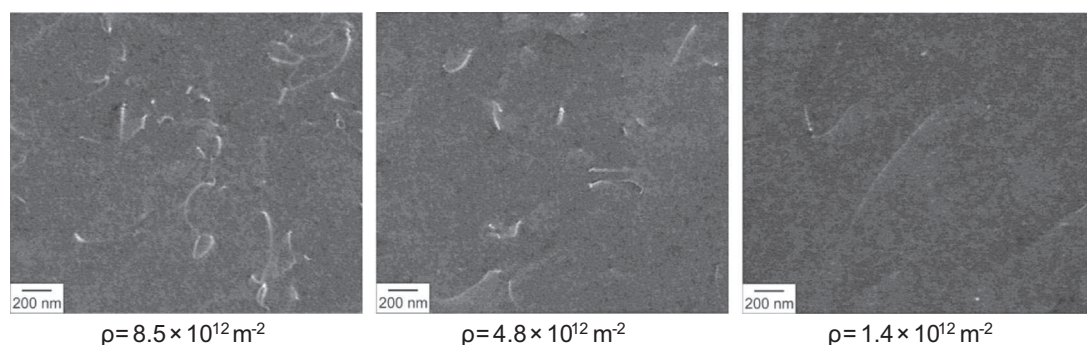
Fig. 1. ECC images of the undeformed material obtained under multi-beam channeling conditions for randomly selected crystal orientations, displaying different dislocations densities, ρ. The left image shows the largest observed density, the right one the smallest.

indent into (001)



indent into (011)

indent into (111)
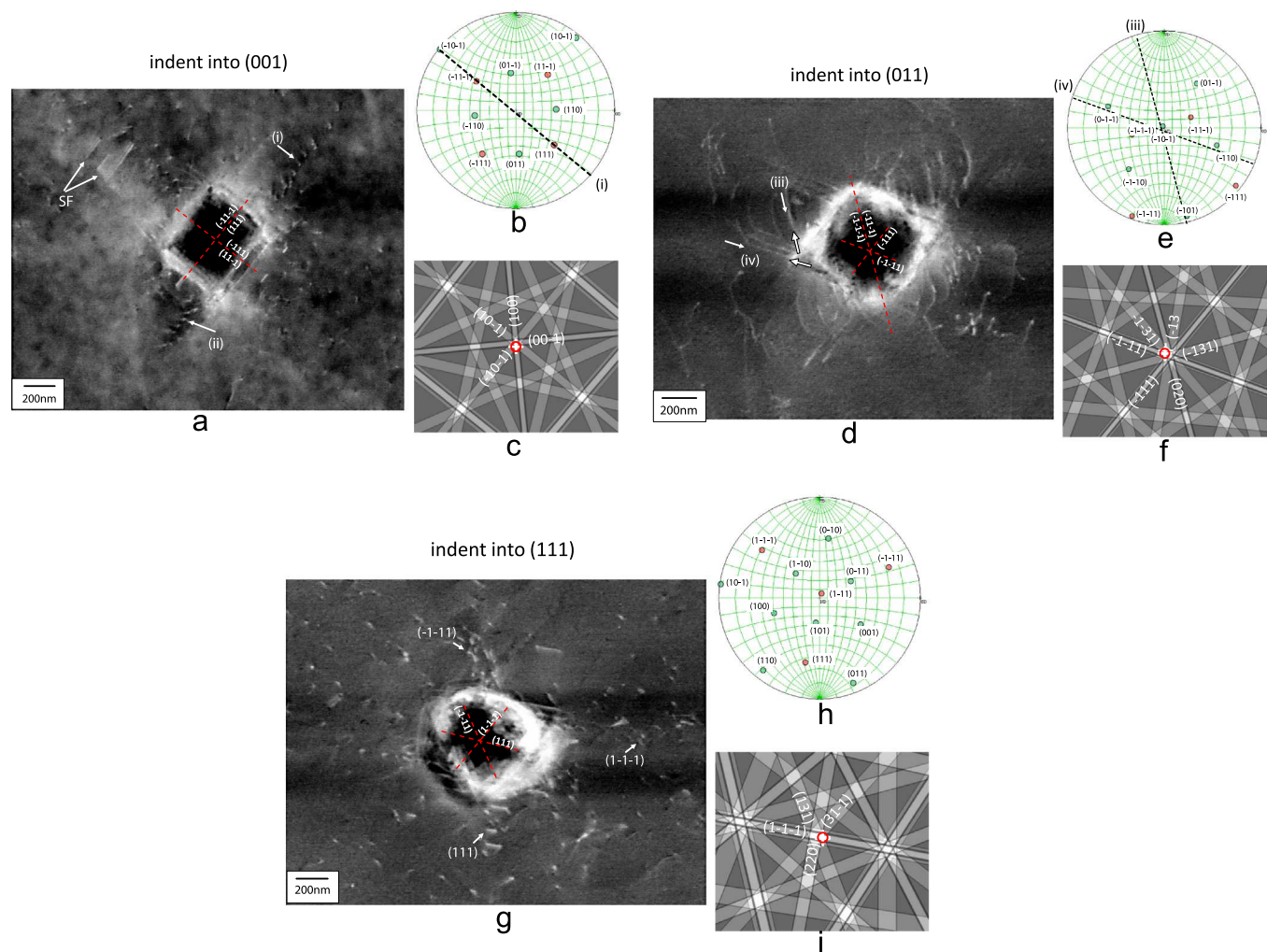
Fig. 2. ECC images of discrete dislocation patterns, imaging conditions (displayed in simulated electron channeling patterns) and stereographic projections for the indents into a crystal with {100} surface normal ((a) to (c)), with {110} surface normal ((d) to (f)) and with {111} surface normal ((g) to (i)). All defects within visibility depth (50 nm) are imaged due to multi-beam conditions. The plane traces of the {111} planes are plotted as red dashed lines. The longer the trace the more parallel is the plane to the sample surface. Stacking faults (SF) appear as straight bright lines indicating the SF intersection with sample surface. Dislocations appear as straight or curved lines with a bright dot indicating the intersection with the surface. Different arrangements of dislocations in form of pile-ups and loops are enumerated (i) to (iv). In the stereographic projections (b), (e) (h) black dashed lines indicate the line trace of the dislocations in the respectively enumerated dislocation pile-ups. (For interpretation of the references to colour in this figure legend, the reader is referred to the web version of this article.)

oriented surfaces. All ECC images in Fig. 2, but also those in Figs. 5 and 6, show almost constant brightness of the matrix crystal, indicating that no significant lattice curvature occurs in the observed surrounding of the indents. This is in line with the observations of Zaafarani et al. [3,4], who showed that large lattice rotations only occur directly below the indent. The ECCI images show no useful information in the area directly below the indent, first because of the significant surface curvature and second because of the high density of dislocations and the associated high lattice rotations.

The stereographic projections corresponding to the ECC images are shown in Fig. 2b, e and h, and the simulated electron channeling patterns indicating the applied diffraction conditions are shown in Fig. 2c, f and i. The traces of all {111} planes are plotted as red dashed lines into the ECC images. A longer trace line indicates a plane more parallel to the sample surface. The poles of the {111} planes are marked red in the stereographic projections. The dislocation patterns reveal four- and two-fold symmetries for the {100}- and {110}-oriented crystals. For the {111}-orientation, dislocations appear randomly distributed and no clear symmetry can be observed, at first instance. A closer look on Fig. 2g after background subtraction to remove some of the strong surface
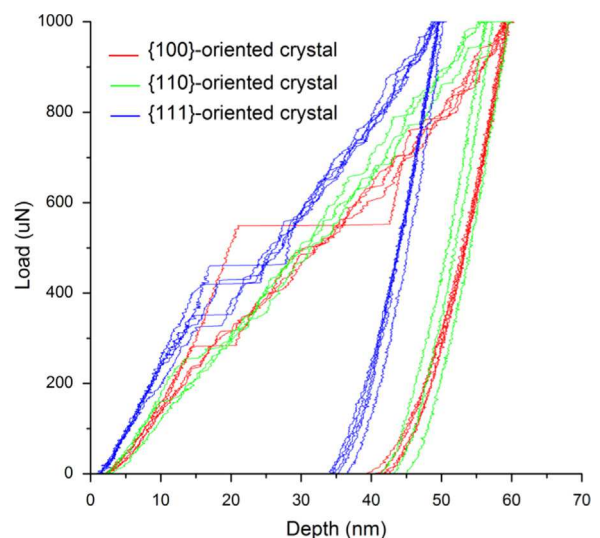
Fig. 3. Load–displacement curves of the nanoindentation tests performed in load-controlled mode with the maximum load of 1000 μN for the {100}-, {110}- and {111}-oriented crystals.
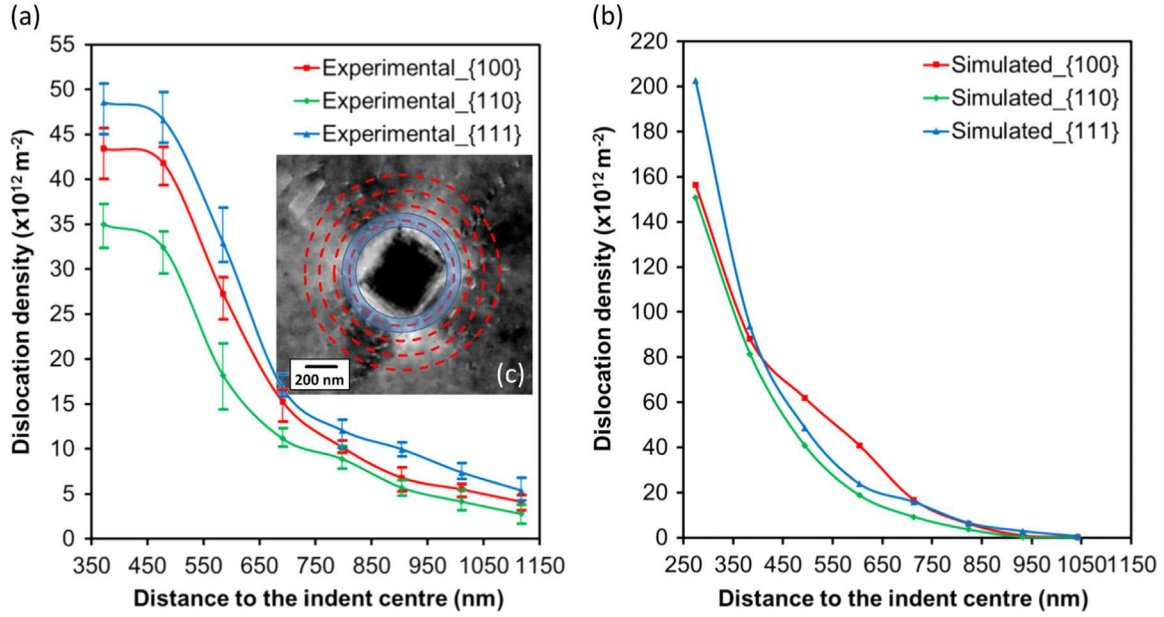
Fig. 4. Dislocation density distributions as a function of the distance to the indent centre calculated from (a) the experiments (error bars indicate minimum, maximum and mean value obtained from 3 different indents) and (b) the DDD simulations. (c) Principle of dislocation density measurement on the example of an (001)-indent: the red circles indicate distances of 350, 450, 550 and 650 nm. Each circle marks the centre of a ring, marked in blue, inside of which the number of dislocations is counted. This number is divided by the ring area. (For interpretation of the references to colour in this figure legend, the reader is referred to the web version of this article.)
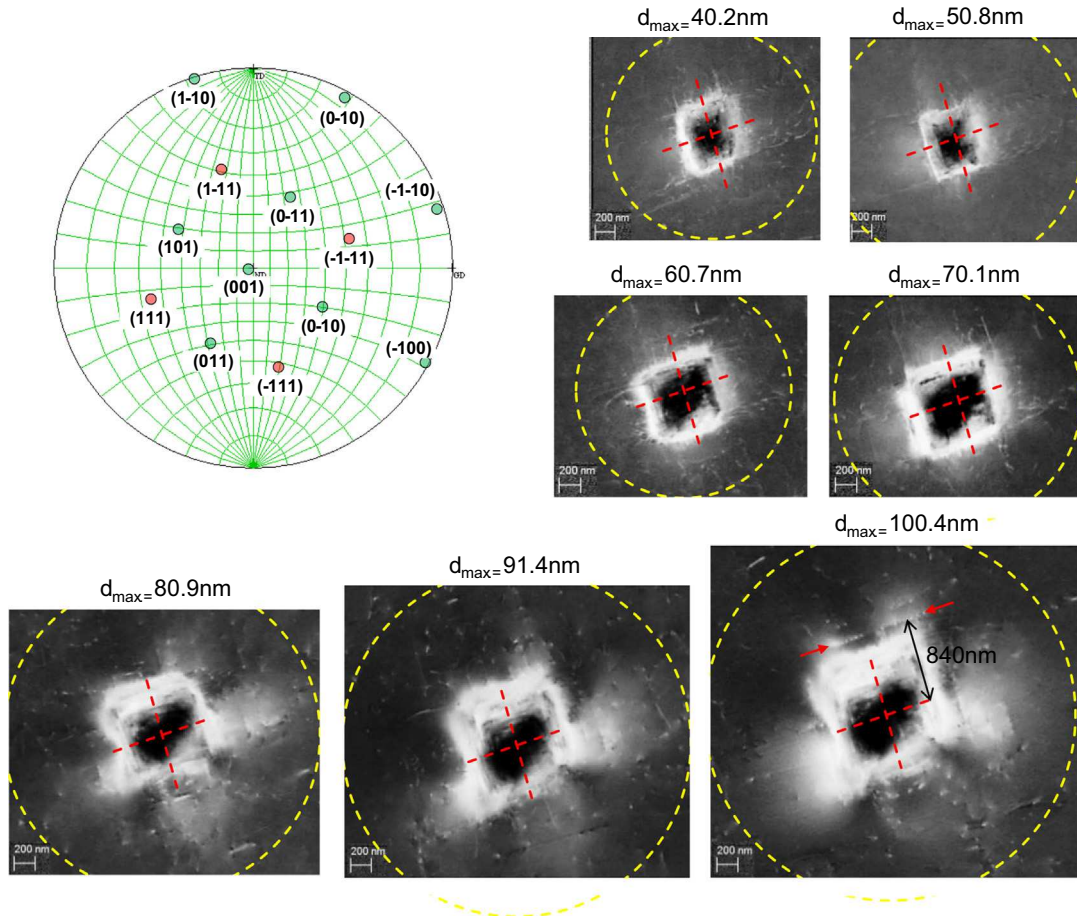
Fig. 5. ECC images of the dislocation patterns around nanoindents indented to different maximum depths between 40 nm and 100 nm in the {100}-oriented crystal. The traces of 4 {111} planes are plotted as red dashed lines as in Fig. 2. The spread of the plastic deformation zone measured as the distance from centre of the indent to the most remote defect of the pattern is indicated by dashed yellow circles. (For interpretation of the references to colour in this figure legend, the reader is referred to the web version of this article.)

curvature contrast, however, reveals a 3-fold symmetry. From the load–displacement curves shown in Fig. 3, nanoindentation into the {111}-oriented crystal shows a larger slope than the other two orientations which we interpret as higher strain hardening rate.

Since the maximum indentation depth obtained in load-controlled mode is only in the order of 50–60 nm, only a small amount of deformation is present in the vicinity of the indent. No twinning or secondary slip has been observed in the ECC images. Thus, the material deforms exclusively on the primary slip systems. Therefore all patterning dislocations lie on {111} planes.

For the {100}-oriented crystal, the 4 {111} planes stand symmetrically under an angle of 54° with respect to the surface plane. Some of the dislocations lying on the right upper side of the indent in Fig. 2a are aligned along the trace of $(\bar{1}1\bar{1})$ lattice plane. They form a dislocation pile-up, indicated as (i). The projected length of the dislocations in pile-up (i) is around 40 nm, and the related line trace (black dashed line in Fig. 2b) is passing through the pole of $(\bar{1}1\bar{1})$ plane. This indicates that these dislocations run perpendicular to the intersection of their slip plane with the surface. From the known inclination of the $(\bar{1}1\bar{1})$ plane (54.7°) and the visible length of the dislocation trace (40 nm) the visibility depth of ECCI was calculated as 40 nm $\times \tan 54.7° \approx 56$ nm. This matches with the value provided by Zaefferer and Elhami [20] for an acceleration voltage of 15 kV and iron as sample material. A second dislocation pile-up (labelled as (ii) in Fig. 2a) can also be seen on the opposite side of the indent.

For the {110}-oriented crystal, two of the 4 {111} planes stand under an angle of 35° with respect to the surface. Another two stand almost perpendicular to the surface plane. Concentric dislocation partial loops can be observed along the four directions indicated by the two shorter plane traces in Fig. 2d. One of these dislocation arrangements, indicated as (iii), is selected as an example for further analysis. These dislocation half loops are embraced by parallel straight lines indicated (iv) in Fig. 2d. These lines are lying parallel to the traces of the $(\bar{1}\bar{1}1)$ planes which are steeply inclined with respect to the sample surface. Any defect on such planes must appear as straight bright line or as single spot in the ECC image. Because the ECC image is not only revealing

crystallographic defects but also surface steps, the nature of these straight lines cannot be unambiguously decided on the basis of ECCI alone.

On the {111}-indented surface shown in Fig. 2g, most of the defects appear as short bright lines, corresponding to either dislocations or stacking faults. For this orientation, 3 {111} planes are standing symmetrically under an angle of around 70° with respect to the surface plane. As previously indicated a visibility depth of about 60 nm was obtained for ECCI in the present case. Thus, a long and most steeply inclined dislocation on one of these {111} planes should have a projection length of around 20 nm which would make them appearing just as bright dots (Fig. 2g). Note, that the best resolution which has been reported for ECCI is in the order of 10 nm [20]. In contrast to the spot-like dislocations, stacking faults should appear as straight bright lines running parallel to the intersection of the stacking fault plane with the surface. With this knowledge we can interpret most of the defects in Fig. 2g as stacking faults lying on all 3 {111} plane traces as indicated in the figure. Besides the short dislocations and stacking faults, some dislocation loops are also observed very close to the indent. They are lying on $(1\bar{1}1)$ planes which are parallel to the sample surface.

Besides characterisation of individual dislocations ECCI also allows for the quantification of the local dislocation density, simply by counting the dislocations found on a particular surface. The results obtained for all three orientations are shown in Fig. 4a as a function of the distance to the indent centre. The results were obtained, as indicated in Fig. 4c by selection concentric rings of equal width around the centre of the indent, counting the amount of dislocation-surface intersections for each ring and then dividing this number by the ring area. As each dislocation loop has two intersections with the surface the counted number of dislocation intersections was divided by 2. For each orientation the dislocation density was measured around 3 indents. The error bar at each point in Fig. 4a indicates the minimum, maximum and average density obtained from these 3 measurements. The error bars are slightly smaller than the density variation measured on the undeformed material, simply because only indents with low
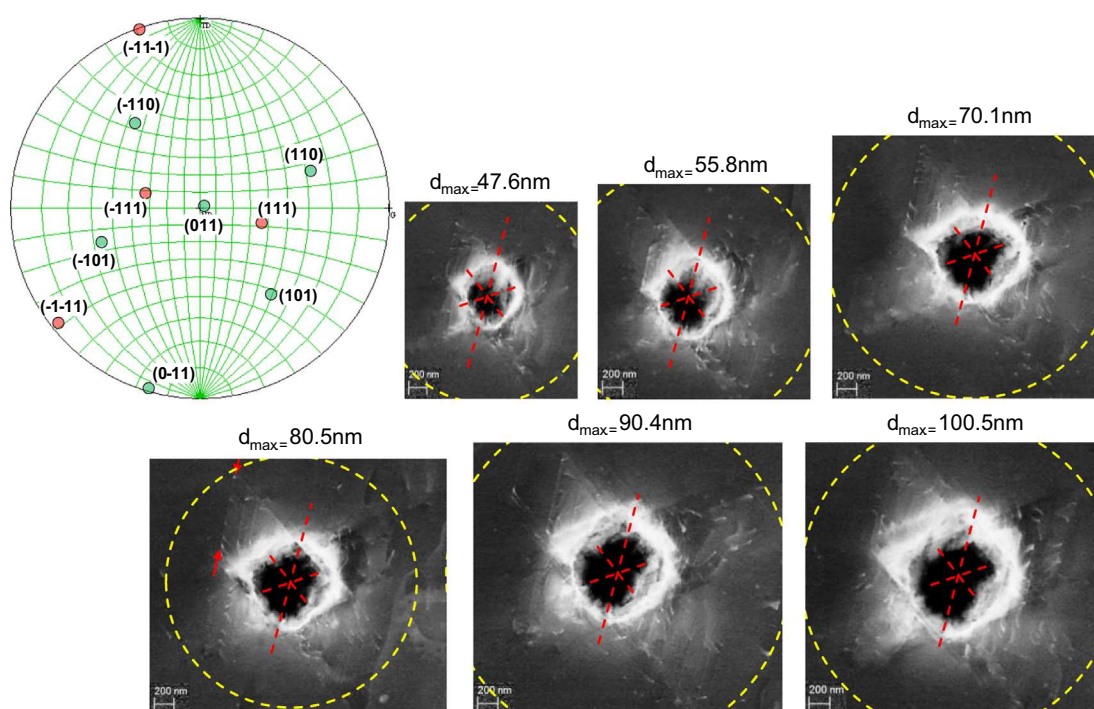

Fig. 6. As Fig. 5 but for the {110}-oriented crystal. (For interpretation of the references to colour in this figure legend, the reader is referred to the web version of this article.)

surrounding dislocation densities were selected. As mentioned above the dislocation density measured as line length per volume is approximately twice as high. As already mentioned, the area below the indenter shows strong topographic contrast and a dislocation density significantly higher than that which can be revealed by ECCI (the limiting dislocation density is about 10^{14}). Therefore, dislocation densities can only be evaluated from a distance larger than 350 nm from the centre of the indent. Furthermore, the densities at the smallest distance to the indent centre in Fig. 4a are smaller than the real densities because of limited visibility. Fig. 4a indicates that the {111}-oriented crystal shows the highest dislocation density and the {110}-oriented the lowest.

3.2. Pattern evolution with increasing indentation depth

Figs. 5 and 6 show ECC images of dislocation patterns around nanoindents indented to different maximum depths between 40 and 100 nm on the {100}- and {110}-oriented surfaces. The images of the {111}-oriented surface are not shown here because the dislocation distribution is too random to be systematically interpreted.

In accordance with the previous results, four- and two-fold symmetries of the dislocation patterns are observed at each indentation depth for the {100}- and {110}-oriented crystals, respectively. Furthermore, by measuring the distance between the centre of the indent and the most remote individual defect created by the indentation process (indicated by the dashed yellow circle), the radius of the plastic deformation zone can be estimated under the assumption that the nanoindentation induced dislocations are all contained in a hemispherical volume below and around the indent. The defects created by indentation were distinguished from those existing before deformation by following the characteristic dislocation pile-up patterns to the most remote ones. The measured distances of the very last remote defect to the centre of the indent are displayed in Fig. 7 by open squares. The contact radius of each nanoindent, extracted from the Hysitron nanoindentation software using Eq. 1, is shown in Fig. 7 by filled squares. The ratio of the radius of the plastic deformation zone to the mathematically fitted contact radius is then computed. As shown in Fig. 7 by filled circles, the obtained ratios are constant around a value of 4.

With increasing indentation depth, new dislocation features appear. For the {100}-oriented crystal dense dislocation pile-ups appear at a distance of approximately 840 nm to the indent centre after an indentation with a maximum depth of 100.4 nm, as marked by red arrows in Fig. 5. These might be residual half loops belonging to one Frank–Read source which was nucleated on a ($\bar{1}11$) plane in the lateral vicinity of the indent. In Fig. 6 the dislocation pile-up also marked by red arrows are the residual fragments of the curved dislocations observed in Fig. 2d. They are aligned along the (111) plane trace.

3.3. Simulation results

For obtaining a deeper insight into the formation mechanisms and the spatial arrangement of the dislocations, DDD simulations of the nanoindentation process were carried out for two cases, one with cross-slip disabled and one with cross-slip enabled. Because of the constrictions in calculation time, the maximum depth of nanoindentation simulation was limited to several tens of Burgers vector lengths corresponding to around 10 nm. Fig. 8 reveals the dislocation pattern within the 100 nm thick slice below the indented surface of the DDD results. For both cases, namely cross-slip disabled and enabled, the dislocations assume four- and two-fold symmetrical patterns for the {100}- and {110}-oriented crystals, and a random scatter of dislocations for the {111}-oriented crystal. A more detailed inspection shows that the cross-slip disabled simulation results fit better to the experimentally observed defect structures. From these data the dislocation density distribution within 100 nm thick slices were determined as a function of the distance to the indent centre using the same approach as that for the experimental data. In contrast to the experiments, only one simulation run was evaluated. The results are plotted in Fig. 4b, using a different scaling as for the graph in Fig. 4a. In general the dislocation densities obtained in the simulations are about 4 to 5 times higher than the experimentally observed values. However, the dislocation density evolution as a function of the distance to the indent centre is very similar for the experimental and simulated data.

4. Discussion

4.1. Defect visibility by ECCI

The visibility of lattice defects by ECCI depends on the correct setting of the channeling conditions. Screw dislocations in an elastically isotropic medium, for example, may become invisible, when the scalar product of the Burgers vector, **b**, and the active
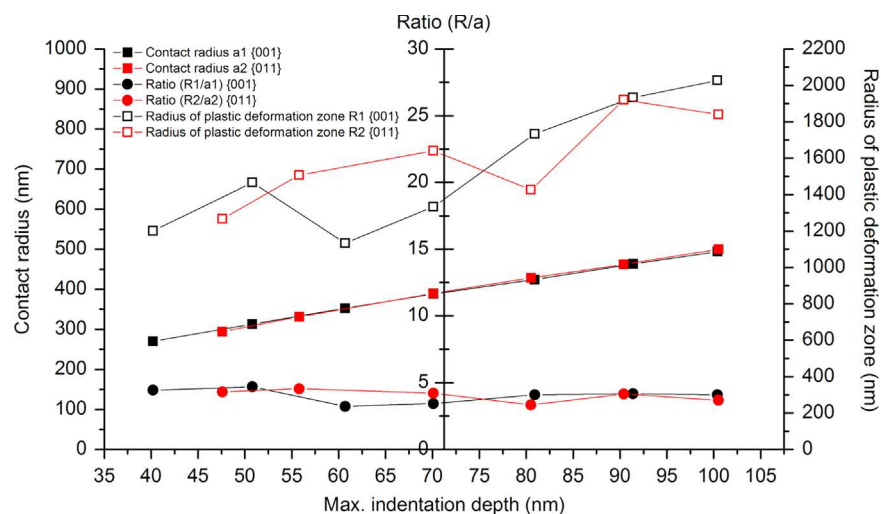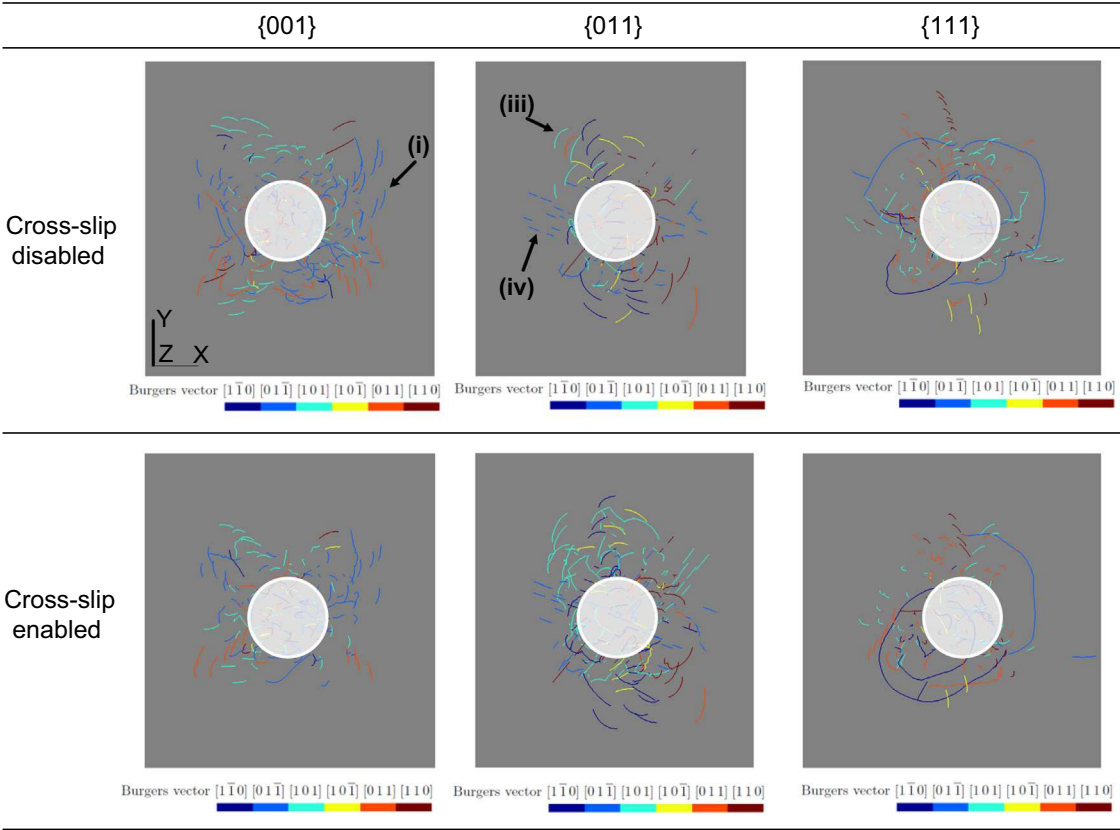

Fig. 7. Plot of the radius of the plastic zone, contact radius and the ratio between them in dependence of the indentation depth for different orientations. The radii of the plastic zones are measured under the assumption that all mobile slip dislocations are constrained within a hemispherical volume.

Fig. 8. Dislocation arrangements obtained by discrete dislocation dynamics (DDD) simulations of nanoindentation into the 3 investigated crystal orientations. Simulations are performed with cross-slip disabled (first row) and cross-slip enabled (second row) conditions. The colours indicate different slip systems. Images correspond to projections of the 100 nm thick slice of the simulated indented surface. This projection is used in order to match the field and depth of view of the corresponding experiments.

diffraction vector, $\mathbf{g}$, is equal to 0:

$$\mathbf{g} \cdot \mathbf{b} = 0.$$

If dislocations are to be observed and their densities determined using ECCI, it is, therefore, of importance to ensure that suitable diffraction conditions have been selected. If the illumination conditions are, accidentally, wrongly selected, dislocations may unexpectedly become invisible and therefore give wrong dislocation density results. Table 1 shows which dislocation types may become invisible under certain diffraction vectors. From this table it becomes clear that, for example, 1/2 of all possible dislocations may be invisible under $\mathbf{g}=(111)$ diffraction conditions, while under $\mathbf{g}=(220)$ only about 1/6 may not be visible. Furthermore, it should be noted that all dislocations having a Burgers vector parallel to the observation direction should be invisible. The latter means that for a given {110} surface normal (Figs. 2(d) and 6) about 1/6 of all possible dislocations may be invisible.

The values for fractions of invisible dislocations mentioned above display the most extreme case and would require that two-beam diffraction conditions are accurately set, the material is elastically isotropic and only screw dislocations are present. However, none of these conditions is fulfilled in the present case; the diffraction conditions are, most probably, multi-beam conditions, the TWIP steel is highly elastically anisotropic and only some of the observed dislocations may have pure screw character. As a result, dislocations are probably always at least slightly visible, provided that good channeling conditions have been selected for the matrix crystal. An uncertainty of dislocation visibility should lead to an uncertainty in dislocation density determination in the order of about 20%. All absolute values displayed in Fig. 4(a) may, therefore, be about 20% higher.

Table 1
Values of $\mathbf{g} \cdot \mathbf{b}$ (g: active diffraction vector, b: Burgers vector). Dislocations may become invisibility or almost invisible if $\mathbf{g} \cdot \mathbf{b}=0$.

g	1 1 1	2 2 0	2 0 0
b			
1 1 0	2	4	2
1 0 1	2	2	2
0 1 1	2	2	**0**
1 $\bar{1}$ 0	**0**	**0**	2
1 0 $\bar{1}$	**0**	2	2
0 1 $\bar{1}$	**0**	2	**0**

It has become clear from the discussion above that the here used technique for obtaining 2-beam conditions is not the optimum, as it does not give absolute certainty on the channeling conditions. Recently, Mansour et al. [31] proposed an elegant way to obtain channeling patterns even on a Zeiss Gemini-type microscope which is not originally designed for this. Although these patterns are of small angular width, the combination with the EBSD-based method used by the present authors [20] allows the exact setting of diffraction conditions.

Another limit for defect visualisation by ECCI is the occurrence of surface relief at the centre of the indent and the overlap of strain fields of individual dislocations close to the centre of the indent. Therefore only those dislocations outside of the centre region of indentation can be observed and quantified. This is, of course, a serious limitation for observation and interpretation of the deformation pattern of an indent. One consequence of this is that the observed dislocation density in Fig. 4(a) saturates close to the indent. As the simulated data show, the dislocation density should rather increase steeply; in fact the

experimental results are erroneous due to fading visibility of dislocations at that area close to the indent. For visualisation of defects directly below the indenter various techniques have been used in the literature, for example careful chemical polishing of the sample surface, combined with observation of the dislocation-related etch pits [32]. This technique delivers high resolution images of the dislocation-surface intersections all the way to the centre of the indent. While in [32] the observations were carried out on MgO, Sadrabadi et al. [33] successfully applied a similar etch-pit technique to image the dislocation structure underneath the indenter in CaF_2 single crystals.

For the case discussed in the present paper, the largest problem for application of such a technique appears to be, besides finding a proper etchant, the high dislocation density formed directly below the indent. The density of geometrically necessary dislocations (GND), ρ_{GND}, below the indent can be estimated from the local orientation gradient measured by 3D EBSD or similar techniques using the rough approximation $\rho_{GND} = c \cdot \Delta\theta/(L \cdot b)$ where $\Delta\theta$ indicates the misorientation that accumulates along the distance L, b is the length of the Burgers vector of the dislocations creating the orientation gradient, and c is a geometry constant of the order of 2 to 5 (see [34] for more details). From 3D EBSD measurements done in our own group [3] and comparable measurements by others (e.g. [35]), we estimate with $\Delta\theta = 10°$ and $L = 3$ μm a density of GNDs in the order of 4–10×10^{14} m^{-2}, corresponding to 400–1000 dislocation intersections per square-micrometre, not yet considering the non-GND types. This appears hardly being resolvable by an etch pit technique. It would also not be resolvable by ECCI and even not by TEM and is probably the reason why TEM observations of the area below the indent often do not resolve individual dislocations [36]. It appears that the best technique for measurement of such high densities of geometrically necessary dislocations (i.e. $\rho_{GND} \geq 10^{14}$ m^{-2}) is orientation microscopy, based on EBSD, TEM or synchrotron X-ray diffraction (e.g. [37,38]).

4.2. Comparison of pattern symmetries obtained by experiments and simulations

Visual comparison of the arrangements of dislocations obtained by experiments (Fig. 2a, d and g) and DDD simulations (Fig. 8) reveals better agreement with the cross-slip disabled condition than that with the cross-slip enabled one for all three orientations. This is consistent with the low stacking fault energy of the here investigated TWIP steel, which leads to a wider dislocation dissociation and prohibits cross-slip [39]. It should be mentioned, however, that the visual comparison is not rigorous. There are two factors which cannot be ignored. Firstly, a scale difference exists. The maximum depth of the simulated nanoindents reaches only around 10 nm, while the depths in the experiments are larger than 40 nm. Secondly, differences in the dislocation nucleation processes strongly influence the dislocation densities present in both cases. Although the here used multi-beam rather than two-beam illumination conditions should render most dislocations visible within the depth of the ECC, a much lower defect density is observed in the experiments as compared with the simulations. This is because 48 Frank–Read sources (4 for each slip system) were used in the model as nuclei in the DDD simulations. In the experiments the number of dislocation nuclei present in the probed volume before the indentation test is most likely much smaller and hence not comparable to the number used in the simulation model. The average defect density before nanoindentation is 1.0×10^{13} m^{-2} taken the average line length per volume density. At the same time the average contact area, calculated by the contact area extracted from the Hysitron nanoindentation software for each indent, is around 3.2×10^5 nm^2. If one assumes that all dislocation nucleation happens at pre-existing dislocations within the contact area between the sample surface and the indenter, the calculated number of sources present before nanoindentation is 2. This is therefore approximately almost 25 times smaller than the number of sources in the simulations. Indeed, most of the dislocation nucleation in the experiment happened *during* nanoindentation. The motivation for using a higher number of potential dislocation sources in the model was to ensure sufficient dislocation activity already at low deformations leading to early stage pattern formation.

The movement of dislocations, in principle, leads to the shear and relative transport of material, in the present case out of the indented area into the surrounding. Different densities of dislocations hence indicate different amount of material transported. Topographical pile-ups are created by dislocations moving out of the surface. The symmetry of the dislocation pattern therefore corresponds to the symmetry of the pile-up. All observed dislocation pattern symmetries show a good match with the surface topographical pile-up pattern symmetries reported in other works from both AFM observation and FEM simulation with large depths [9,11].

4.3. 3-dimensional dislocation geometry and dislocation type determination

Similar to TEM, ECC images of dislocations display a projection of the dislocation lines, with the difference that the projection in
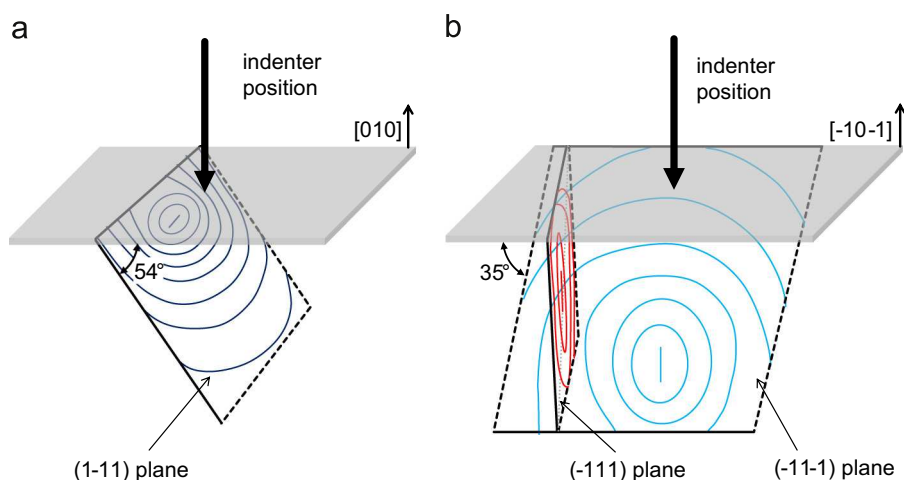
Fig. 9. 3-dimensional schematics of the configurations of (a) the dislocation pile-up (i) and (ii) for the {100}-oriented crystal (shown in Fig. 2a), and (b) the dislocation partial loops (iii) and dislocation lines (iv) for the {110}-oriented crystal (shown in Fig. 2d). (For interpretation of the references to colour in this figure legend, the reader is referred to the web version of this article.)

ECC usually takes place over a smaller interaction depth. Advantageous with respect to TEM is the asymmetric appearance of dislocation lines: the intersection of the lines with the sample surface is marked by bright spots which makes it easy to recognise which side is up and which down. This allows the determination of the line inclination with respect to the surface without further tilting experiments. From the known crystallographic direction of the line trace, thus, the crystallographic line direction can be estimated [20]. In this paper we use the combination of ECCI observation and DDD simulation to reveal the 3D geometries of the dislocation arrangements.

Fig. 9 sketches the 3D geometries of three sets of dislocations observed in the dislocation patterns on the {100}- and {110}-oriented surfaces. Fig. 9a shows the geometry of the dislocation pile-ups (i) and (ii) in Fig. 2a. As previously described, the dislocations are piling up along a trace of the $(\bar{1}1\bar{1})$ lattice plane, which has an inclination angle of around 54° with respect to the surface plane. This suggests that these dislocations were formed from one source. A similar arrangement of dislocations was also found in the DDD simulation results, indicated also as (i) in Fig. 8. As the load increases, the number of dislocation loops initiated by the source also increases. When segments of these loops reach the surface, they disappear and leave behind residual dislocations visible in the form of dislocation pile-ups.

The dislocations (iii) in Fig. 2d are fading out at both ends, indicating that the loops bend towards the sample surface as shown by the blue dislocation loops in Fig. 9b. These dislocation loops are formed by activation of one primary slip source on one $(\bar{1}1\bar{1})$ plane, which has an angle of around 35° with respect to the surface plane. The simulation results show similar arrangements of dislocations, indicated as (iii) in Fig. 8. The dislocation loops at the periphery move on one side towards the sample surface, on the other side down into the material. As soon as the loop touches the surface, it moves out and opens the full loop. In the ECC image, this is visible by two bright dots connected with fading dislocation lines, as shown in Fig. 6 by dislocation pile-ups marked within the red arrows. Additionally in Fig. 6 dislocation pile-ups parallel to the one marked with red arrows indicate that the same type of Frank–Read sources appear on several parallel planes.

The traces of the dislocation lines (iv) in Fig. 2d indicate that these dislocations are lying on the $(\bar{1}1\bar{1})$ plane. Since this plane is observed almost perfectly edge-on, every dislocation appears as a straight line in the ECC image. This observation can be interpreted in two ways: either the lines correspond to dislocation loops as indicated in the schematic drawing given by the red lines in Fig. 9b, or the lines correspond to single straight dislocation segments running almost parallel to the surface. The results from

DDD, indicated by (iv) in Fig. 8 suggest that the lines are rather projections of dislocation loops.

4.4. Mechanisms of pattern formation

Based on sufficient understanding of the dislocation geometries and types, the formation of the total pattern symmetry can be considered. Fig. 10 demonstrates the slip systems and possible areas where the dislocations might show up in an ECC image for each orientation studied. Each colour represents a defined slip plane. For those slip planes which are standing relatively steeply inclined with respect to the surface the dislocations are seen as pile-ups along {111} plane traces. They are drawn in Fig. 10 as narrow ellipses parallel to the plane trace. This concerns the four 54° inclined {111} planes in the {001}-oriented crystal (indicated by dark blue lines in Fig. 9a), the two 90° inclined planes in the {011}-oriented crystal (indicated by red lines in Fig. 9b) and three 70° inclined {111} planes in the {111}-oriented crystal. There are four exceptional slip systems in the {011}-oriented crystal, namely $(\bar{1}1\bar{1})[0\bar{1}\bar{1}]$, $(\bar{1}1\bar{1})[\bar{1}\bar{1}0]$, $(\bar{1}\bar{1}\bar{1})[01\bar{1}]$ and $(\bar{1}\bar{1}\bar{1})[110]$, in which the particular ⟨110⟩-type slip directions also play a significant role. Because the two involved slip planes stand under a shallow angle of around 35° with respect to the surface, the dislocations emitted from the corresponding Frank–Read sources are firstly seen as partial loops in ECC images (indicated by blue lines in Fig. 9b). In this case, the dislocations leave surface steps along the slip directions and tend to form clear geometrical patterns as shown by wider ellipses in Fig. 10b.

As previously indicated, the {111}-oriented crystal shows a very different behaviour, including larger strain hardening rate and no clear dislocation patterning in contrast to the other two orientations. In contrast to these observations on TWIP steel, the nanoindentation load–displacement curves obtained on copper single crystals show the same strain hardening rate for all three orientations [11]. This indicates that the cross-slip inhibition in TWIP steel is playing an essential role for the work hardening of the material during nanoindentation. The different work hardening rate of the different orientations may be explained as follows: because the indents in this study are all very shallow, their stress field is comparable to that of uniaxial compression. As shown in Fig. 11, the shear stress on the {111} plane, standing under 70° with respect to the sample surface in the {111}-oriented crystal, is larger than the shear stress on the {111} plane which stands under 54°. This leads, on the one hand, to a quicker activation of Frank–Read sources followed by a larger dislocation density increase underneath the indenter in the {111}-oriented crystal. On the other hand, the dissociated dislocations quickly
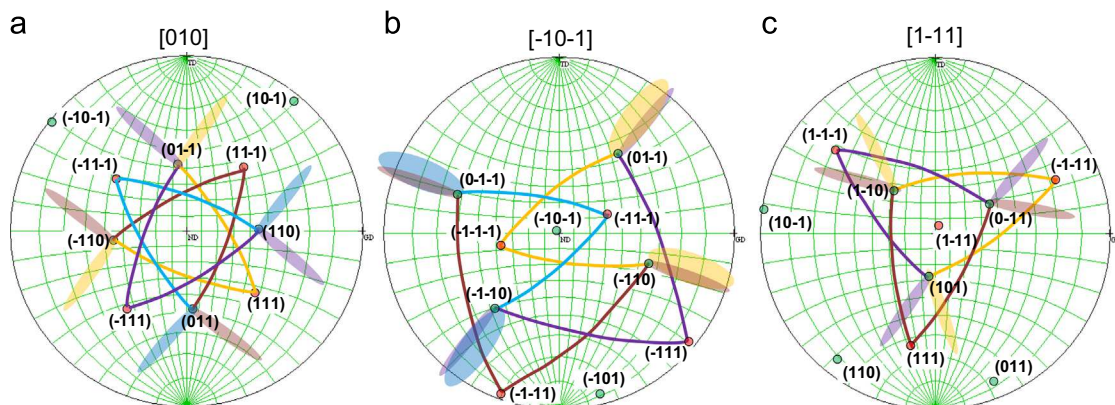

Fig. 10. Overlay of actual dislocation patterning positions on the stereographic projections of the 3 investigated crystal orientations. Different colours represent primary slip systems on different {111} planes. Ellipses represent the positions in ECC images where the dislocation patterns might appear. Narrow and wide ones represent the dislocation patterning appearance of pile-ups and parallel dislocation loops. Note that the ellipses are plotted in real space and not in the angular space of the stereographic projection.

form a network of immobile dislocations because cross-slip is inhibited. These two mechanisms are the reasons why the strain hardening rate in the {111}-oriented crystal is larger. Fig. 4 reveals the distributions of the dislocation density in both experimental and simulation results as a function of the distance to the indent centre for all three orientations. In comparison to the {100} and {110} indents, the {111} indent starts with a higher dislocation density in the region closer to the indent and drops more quickly. This supports the hypothesis put forward above. The strong interaction between high densities of dislocations decreases the dislocation patterning effect. In addition, the dislocations lying on 70° inclined planes appear as bright dots or very short white lines in ECC images. These two aspects are responsible for the random appearance of the dislocation patterns in Fig. 2g.

4.5. Size of plastic deformation zone prediction by contact radius

When dealing with deformation constraint to small volumes it is regularly observed that the strength of a plastically deformable material increases with decreasing size of the deformed volume. In case of nanoindentation this effect is called the indentation size effect and it strongly influences the interpretation of nanoindentation experiments, see e.g. [40,41]. Nix and Gao developed a model (N–G model) by considering the geometrical necessary dislocations generated in the material under a conical indenter [14]. In this model it was assumed that the GNDs induced by pressing the indenter into the material are constrained to an approximately hemispherical volume below the region of contact. This hemispherical volume was also assumed to scale with the contact radius [42].

Motivated by the N–G model we measured the radius of the hemisphere which contains all the visible dislocations produced during indentation using the ECC images. We emphasise here that the dislocations shown in Figs. 5 and 6 are not only static GNDs but a large fraction of them are mobile slip dislocations. This means that the radius measured from an ECC image is a very precise measure of the true spread of the plastic deformation zone. Following the N–G model, the ratio between the radius of the actual plastic zone and the mathematically fitted contact radius was calculated. It turns out that the ratios are around a constant value of 4 as shown in Fig. 6 by filled circles for {100}- and {110}-oriented crystals. As described previously for the results of the DDD simulations, the size of the plastic deformation zone for the {111}-indented surface is slightly larger than that of the other two orientations. Therefore, a factor of 4 may not hold for the {111}-orientation.
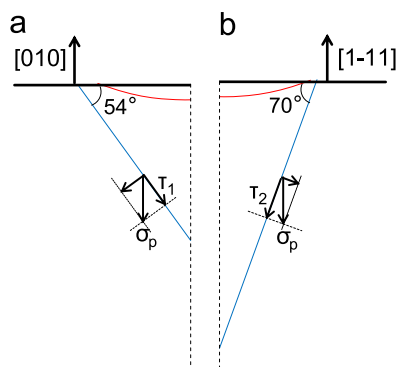
Fig. 11. Sketch of the major shear stress vectors for the {001}- and {111}-oriented crystals obtained under the assumption that most of the material underneath the indenter is under uniaxial compression with a principal normal stress σ_p The shear stresses τ act on the {111} planes standing at an angle of (a) 54° or (b) 70° with respect to the sample surface are shown.

In the original Nix–Gao model, derived for conical indenters, the ratio of the size of the plastic zone to the size of the indenter surface is equal to 1, i.e. the diameter of the deformation hemisphere is assumed to be as large as the indented surface diameter. For spherical indenters, the relationship turns out to be more complicated and depends on the depth of the indent and the size of the indenter, as shown by Swadener et al. [43]. These authors showed that for very small spheres the Nix–Gao model significantly overestimates the strength. One correction for this is to assume that the radius plastic zone is actually larger than that of the indent surface, due to the fact that GNDs of similar sign, collected in the indented volume, will effectively repel each other and, therefore, increase the plastically deformed volume. A similar proposal was also made by Durst et al. [44], however, for conical indenters. These authors proposed a diameter ratio of 1.5 to 2.5. Our own findings of a value of about 4 are in quite good agreement with all the above discussed deviations from the NG model. The reason for our relatively large value may be that the ECCI technique actually reveals every single dislocation even in areas of very low densities where their effect on the material strength may be negligible. Indeed, as suggested by the data in Fig. 4, the highest dislocation densities are measured up to a radius which is about half as large as the total radius (i.e. in Fig. 4, 750 nm instead of 1150 nm). With this we would propose an effective size ratio of about 2 to 3, in very close agreement with the data mentioned by Durst et al. [44].

5. Conclusions

In this paper detailed observations of discrete dislocation patterns around nanoindents using electron channeling contrast imaging under controlled diffraction conditions (cECCI) are presented. cECCI is a powerful tool for visualising crystal lattice defects in bulk materials and obtaining their associated comprehensive crystallographic characteristics. Here cECCI is used for the first time to study defects created during nanoindentation into a bulk TWIP steel sample. The investigated material has fcc crystal structure and a low stacking fault energy. Selected crystals of a polycrystalline sample were studied. We draw five main conclusions:

1. Four- and two-fold symmetric discrete dislocation patterns around nanoindents are observed for the {100}- and {110}-oriented crystals, respectively. The dislocations around the {111}-oriented crystal show 3-fold symmetry which is, however, more difficult to observe than that of the other orientations. For the here studied maximum indentation depth of 100 nm, slip occurs exclusively on primary slip systems.
2. It is difficult to understand the 3D arrangement of dislocations from the ECCI observations alone. However, with the assistance of discrete dislocation dynamic (DDD) simulations the arrangement could be fully explained.
3. Significant differences are observed with respect to the total dislocation densities between simulation and experiment. They can be related to the significantly lower amount of dislocation sources in the initial state of the experiment. The comparison between experiment and simulation further reveals that the low-stacking fault energy TWIP steel deforms, as expected, without cross-slip.
4. The {111}-oriented crystal shows a larger strain hardening rate and a more random pattern formation than the other two indented orientations. This behaviour is in contrast to, for example, indentations into copper where all three orientations show similar strain hardening behaviour. We propose this difference to be due to the restricted cross-slip in TWIP steels

which leads to dislocation pile-up stresses on the most active slip systems. The {111}-orientation has 3 slip planes with high resolved shear stresses, whereas the other orientations have less or lower stressed slip planes.

5. With increasing indentation depth the dislocation patterns develop in a self-similar manner with increasing lateral extension. The ratio of the radius of the plastic deformation zone to the contact radius stays constant with a value of about 4 independent of indentation depth and orientation. This result is in good agreement with an extended Nix–Gao model ([x]) and allows the estimation of the size of the plastic zone around an indent simply from its contact radius.

Acknowledgements

References

[1] A.C. Fischer-Cripps, Nanoindentation, Springer, Lindfield, Australia, 2004.
[2] G.M. Pharr, W.C. Oliver, F.R. Brotzen, J. Mater. Res 7 (1992) 613.
[3] N. Zaafarani, D. Raabe, R.N. Singh, F. Roters, S. Zaefferer, Acta Mater. 54 (2006) 1863.
[4] N. Zaafarani, D. Raabe, F. Roters, S. Zaefferer, Acta Mater. 56 (2008) 31.
[5] M.C. Fivel, C.F. Robertson, G.R. Canova, L. Boulanger, Acta Mater. 46 (1998) 6183.
[6] A.M. Minor, E.T. Lilleodden, E.A. Stach, J.W. Morris, J. Electron. Mater. 31 (2002) 958.
[7] K.W. McElhaney, J.J. Vlassak, W.D. Nix, J. Mater. Res. 13 (1998) 1300.
[8] K.A. Nibur, D.F. Bahr, Scr. Mater. 49 (2003) 1055.
[9] Y. Wang, D. Raabe, C. Klüber, F. Roters, Acta Mater. 52 (2004) 2229.
[10] Y. Liu, B. Wang, M. Yoshino, S. Roy, H. Lu, R. Komanduri, J. Mech. Phys. Solids 53 (2005) 2718.
[11] Y. Liu, S. Varghese, J. Ma, M. Yoshino, H. Lu, R. Komanduri, Int. J. Plast. 24 (2008) 1990.
[12] B. Eidel, F. Gruttmann, Comput. Mater. Sci. 39 (2007) 172.
[13] C. Zambaldi, F. Roters, D. Raabe, U. Glatzel, Mater. Sci. Eng. A-Struct. Mater. Prop. Microstruct. Process. 454 (2007) 433.
[14] W.D. Nix, H. Gao, J. Mech. Phys. Solids 46 (1998) 411.
[15] N.I. Tymiak, D.E. Kramer, D.F. Bahr, T.J. Wyrobek, W.W. Gerberich, Acta Mater. 49 (2001) 1021.
[16] M. Rester, C. Motz, R. Pippan, Philos. Mag. Lett. 88 (2008) 879.
[17] I. Gutierrez-Urrutia, S. Zaefferer, D. Raabe, Scr. Mater. 61 (2009) 4.
[18] M.A. Crimp, Micros. Res. Tech. 69 (2006) 374.
[19] I. Gutierrez-Urrutia, S. Zaefferer, D. Raabe, JOM 65 (2013) 1229.
[20] S. Zaefferer, N.N. Elhami, Acta Mater. 75 (2014) 20.
[21] A. Arsenlis, W. Cai, M. Tang, M. Rhee, T. Oppelstrup, G. Hommes, T.G. Pierce, V.V. Bulatov, Model. Simul. Mater. Sci. Eng. 15 (2007) 553.
[22] Z. Wang, H. Bei, E.P. George, G.M. Pharr, Scr. Mater. 65 (2011) 469.
[23] S. Shim, H. Bei, M.K. Miller, G.M. Pharr, E.P. George, Acta Mater. 57 (2009) 503.
[24] N.I. Kato, Y. Kohno, H. Saka, J. Vac. Sci. Technol. A-Vac. Surf. Films 17 (1999) 1201.
[25] W.C. Oliver, G.M. Pharr, J. Mater. Res. 7 (1992) 1564.
[26] S. Zaefferer, J. Appl. Crystallogr. 33 (2000) 10.
[27] W. Cai, A. Arsenlis, C.R. Weinberger, V.V. Bulatov, J. Mech. Phys. Solids 54 (2006) 561.
[28] B.A. Simkin, M.A. Crimp, Ultramicroscopy 77 (1999) 10.
[29] E. Underwood, in: J. McCall, W. Mueller (Eds.), Microstructural Analysis, Springer, US, 1973, p. 35.
[30] G. Gottstein, Physical Foundations of Materials Science, Springer, Berlin, Heidelberg, 2004.
[31] H. Mansour, J. Guyon, M.A. Crimp, N. Gey, B. Beausir, N. Maloufi, Scr. Mater. 89 (2014) 77.
[32] Y. Gaillard, C. Tromas, J. Woirgard, Acta Mater. 51 (2003) 1059.
[33] P. Sadrabadi, K. Durst, M. Göken, Acta Mater. 57 (2009) 1281.
[34] P. Konijnenberg, S. Zaefferer, D. Raabe, Acta Mater. (2015), submitted for publication.
[35] W. Yang, B.C. Larson, G.M. Pharr, G.E. Ice, J.D. Budai, et al., J. Mater. Res. 19 (2004) 66.
[36] M. Rester, C. Motz, R. Pippan, Philos. Mag. Lett. 88 (2008) 879.
[37] S. Zaefferer, Cryst. Res. Technol. 46 (2011) 607.
[38] L. Wang, M. Li, J. Almer, T. Bieler, R. Barabash, Front. Mater. Sci. 7 (2013) 156.
[39] O. Grässel, L. Krüger, G. Frommeyer, L.W. Meyer, Int. J. Plast. 16 (2000) 1391.
[40] G.M. Pharr, E.G. Herbert, Y.F. Gao, Annu. Rev. Mater. Res. 40 (2010) 271.
[41] A. Gouldstone, N. Chollacoop, M. Dao, J. Li, A.M. Minor, Y.L. Shen, Acta Mater. 55 (2007) 4015.
[42] H. Gao, Y. Huang, W.D. Nix, J.W. Hutchinson, J. Mech. Phys. Solids 47 (1999) 1239.
[43] J.G. Swadener, E.P. George, G.M. Pharr, J. Mech. Phys. Solids 50 (2002) 681.
[44] K. Durst, B. Backes, M. Göken, Scr. Mater. 52 (2005) 1093.